Available online at www.sciencedirect.com
ScienceDirect
Trans. Nonferrous Met. Soc. China 33(2023) 454−466
Transactions of Nonferrous Metals Society of China
www.tnmsc.cn

Effect of volume fraction of 18R-LPSO phase on corrosion resistance of Mg−Zn−Y alloys

Guo-qiang XI[1], Yu MOU[1], Yan-long MA[1], Xu-han ZHAO[1], Ju XIONG[1], Kai MA[2], Jing-feng WANG[2]

1. College of Material Science and Engineering, Chongqing University of Technology, Chongqing 400054, China;
2. College of Materials Science and Engineering, Chongqing University, Chongqing 400044, China

Received 25 October 2021; accepted 28 February 2022

Abstract: This study aims to elucidate the effect of LPSO phases on the corrosion behavior of magnesium alloys through experimental design. The microstructure and corrosion behavior of four Mg−Zn−Y alloys designed according to the minimum structural unit for forming the 18R-LPSO phase, i.e. Zn/Y=3/4 (molar ratio), were studied in a comparative manner. The results showed that the alloys mainly contained α-Mg and 18R-LPSO phases, and the volume fraction of the 18R-LPSO phase increased with the increase of Zn and Y contents. The volume fraction of the 18R-LPSO phase in the four alloys was, in sequence, 16.55%, 34.45%, 54.24% and 70.36%, and the spatial distribution of the 18R-LPSO phase also changed from discrete blocks to continuous networks. When the volume fraction was about 50%, the corrosion resistance of the alloy was the best. When the volume fraction was greater than or less than 50%, the corrosion resistance of the alloy decreased.

Key words: Mg−Zn−Y alloy; 18R-LPSO phase; volume fraction; corrosion resistance

1 Introduction

Magnesium alloy is currently the lightest metal structural material in the world, with its density being about 2/3 that of aluminum alloy and 1/4 that of steel. As a result, magnesium alloys are attractive for structural systems, especially in the aerospace and automotive industry. However, there are many problems in the application of magnesium alloys, such as poor deformability at room temperature, high susceptibility to corrosion attack, and relatively low strength and ductility [1−5]. In recent years, the discovery of long period stacking ordered (LPSO) phases provides an opportunity to solve the key problems of magnesium alloys [6−10].

Mg−Zn−Y alloy system has attracted much attention because of its good casting and mechanical properties. Most importantly, it is one of the typical magnesium alloy systems containing LPSO phases [11,12]. In recent years, much work regarding the strengthening and toughening mechanism of LPSO phases have been carried out to improve the mechanical properties of magnesium alloys. HAGIHARA et al [13] found that, in an extruded Mg97Y2Zn1 alloy, the 18R-LPSO phase (with a volume fraction of 24%) and the (0001) base plane of the alloy matrix were parallel to the extrusion direction, which effectively improved the strength of the alloy. Its strengthening mechanism is comparable to that of short fiber reinforced composite materials. GARCES et al [14] confirmed that, if the load was aligned with the fiber direction (extrusion direction), the elongated fibrous LPSO phase was equivalent to the reinforcement in the metal matrix composite. When subjected to tensile stress, the α-Mg grain could transfer part of the load to the LPSO phase, consequently, the local load on the LPSO phase would be higher than the macroscopic stress imposed on the alloy.

Corresponding author: Yan-long MA, E-mail: myl@cqut.edu.cn; Jing-feng WANG, E-mail: jfwang@cqu.edu.cn
DOI: 10.1016/S1003-6326(22)66119-3

In addition to mechanical properties, researchers recently have also done much work on the relationship between the LPSO phase and the corrosion behavior of magnesium alloys. For instance, LIU et al [15] showed that the LPSO phase could significantly improve the corrosion resistance of Mg−Gd−Zn−Zr alloys. They believed that micro-galvanic corrosion was the main corrosion mechanism of the alloy, and the local potential and the volume fraction of the second phase determined the degree of micro-galvanic corrosion. WANG et al [16] immersed the forged MgGd6Y2Zn1Zr10.3 alloy in 0.1 mol NaCl solution for 120 h and found that the LPSO phase acted as the cathode accelerating the micro-galvanic corrosion, thereby reducing the corrosion resistance of the alloy. SRINIVASAN et al [17] showed that the layered LPSO phase in the as-cast $MgGd_{10}Zn_x$ (x=2, 6 wt.%) alloy promotes the filiform corrosion, resulting in decreased corrosion resistance. WANG et al [18] showed that Mg−Y−Zn alloy with either 18R-LPSO or 14H-LPSO phase has better corrosion performance than alloys with both 18R-LPSO and 14H-LPSO phases.

The literature review suggests that the influence of the LPSO phase on the corrosion resistance of magnesium alloys varies with the alloy system, the type and distribution of the LPSO phase. This is probably why there are many arguments regarding the effect of LPSO phase on the corrosion behavior of magnesium alloys. Therefore, in this work, four Mg−Zn−Y alloys were designed according minimum structural unit for forming the 18R-LPSO phase, i.e. Zn/Y=3/4 (molar ratio) [19,20]. On this basis, the corrosion behavior of the four Mg−Zn−Y alloys, namely $MgZn_{0.5}Y_{0.67}$, $MgZn_1Y_{1.33}$, $MgZn_2Y_{2.66}$ and $MgZn_3Y_{3.99}$, in 3.5 wt.% NaCl solution was comparatively studied. Based on the evolution of the volume fraction and morphology of 18R-LPSO phase in Mg−Zn−Y alloys, the mechanism of LPSO phase on the corrosion behavior of magnesium alloys was discussed.

2 Experimental

2.1 Material preparation

The four different types of Mg−Y−Zn alloys were produced by casting from pure magnesium (purity of 99.99%) and $MgY_{21.5}$ master alloy. According to the design ratio of Zn/Y molar ratio of 3/4 for each batch, the pure magnesium and the master alloy were put into a stainless steel crucible and then heated in a resistance furnace. The CO_2 + SF6 gas mixture was introduced into the entire melting process as a protective atmosphere. The cast alloy was obtained by keeping the melt at 750 ℃ for 25 min and then cooled in a salt water bath. The composition and designation of the as-cast alloys are as follows: $MgZn_{0.5}Y_{0.67}$, $MgZn_1Y_{1.33}$, $MgZn_2Y_{2.66}$ and $MgZn_3Y_{3.99}$ (at.%, denoted as 1#, 2#, 3# and 4# alloys respectively). The specific ingredients are shown in Table 1. Samples for microstructural characterization, electrochemical measurements and immersion tests were prepared from the ingots. Each sample was sequentially ground with sandpapers from 320# to 3000#, ultrasonically cleaned in distilled water, and then dried in cool air.

2.2 Microstructure observation

Samples for microstructural observation were first mechanically ground and then electrochemically polished in commercial ACII solution, under a constant voltage of 20 V, at −30 °C, for ~220 s. The microstructure was observed using Zeiss Sigma HD field emission gun scanning electron microscope (FEG-SEM) equipped with an energy dispersive X-ray spectrometer (EDS). For phase analysis, X-ray diffraction (XRD) with Cu K_α radiation was performed, and MDI Jade 5.0 software was used to analyze the obtained XRD patterns.

Table 1 Chemical compositions of Mg−Zn−Y alloys (wt.%)

Alloy	Zn	Y	Gd	Si	Ca	Fe	Mn	Ni	Mg
1#	1.2933	1.6002	0.0429	0.0354	0.0204	0.0149	0.0119	−	Bal.
2#	2.1952	3.0685	0.0859	0.0463	0.0419	0.0192	0.0117	−	Bal.
3#	4.1962	7.4271	0.1522	−	0.073	0.0234	0.0145	0.053	Bal.
4#	6.5724	10.6979	0.2446	0.036	0.1272	0.0299	0.015	0.0665	Bal.

2.3 Immersion test

The immersion test was carried out in 3.5 wt.% NaCl solution at room temperature. During the immersion process, a stereo microscope (SMZ, SZN71) was used to observe and record the macroscopic corrosion morphology of the sample surface. Further, the hydrogen evolution test and mass loss test were performed on parallel samples immersed in 3.5 wt.% NaCl solution at room temperature for 24 h. The corrosion products of selected samples were removed by immersing the samples in a mixed solution containing 200 g/L chromic acid and 10 g/L of $AgNO_3$ according to the national standard GB/T16545—1996 [21]. The surface and cross-sectional morphology of the samples were observed by FEG-SEM. The cross sections of the samples were prepared by ultramicrotomy (Leica Ultracut).

2.4 Electrochemical measurements

Electrochemical measurements were carried out on a Gamry Reference 3000 potentiostat at room temperature in 3.5 wt.% NaCl solution. The sample, a platinum plate and a saturated calomel electrode were used as the working electrode, counter electrode and reference electrode, respectively. Prior to potentiodynamic polarization and electrochemical impedance spectroscopy tests, the open circuit potential (OCP) of the alloy was measured for a minimum of 5 min to establish an approximately steady state.

3 Results

3.1 Microstructure analysis

Backscattered electron (BSE) micrographs and XRD patterns of the as-cast 1#, 2#, 3# and 4# alloys are shown in Figs. 1 and 2, respectively. As seen in Fig. 1, the alloys are composed of Mg matrix with the dark contrast and second phases with light contrast. According to the XRD analysis shown in Fig. 2, the main second phase is $Mg_{12}ZnY$ (LPSO) phase, and the white particles (indicated by the red ellipses) are $Mg_{24}Y_5$ phase. According to the literature [22], the LPSO phase in the selected alloy system is 18R type. The morphology of the 18R-LPSO phase changed gradually from discrete blocks to continuous networks with the increase of Zn and Y contents. The volume fractions of the 18R-LPSO phase in the four alloys were estimated to be 16.55%, 34.45%, 54.24% and 70.36%, respectively.

3.2 Corrosion behavior during immersion test

Figure 3 shows surface morphology of the alloys recorded in-situ when they were immersed in 3.5 wt.% NaCl solution for 2, 10, 30 and 60 min, respectively. After immersion for 2 min, there were

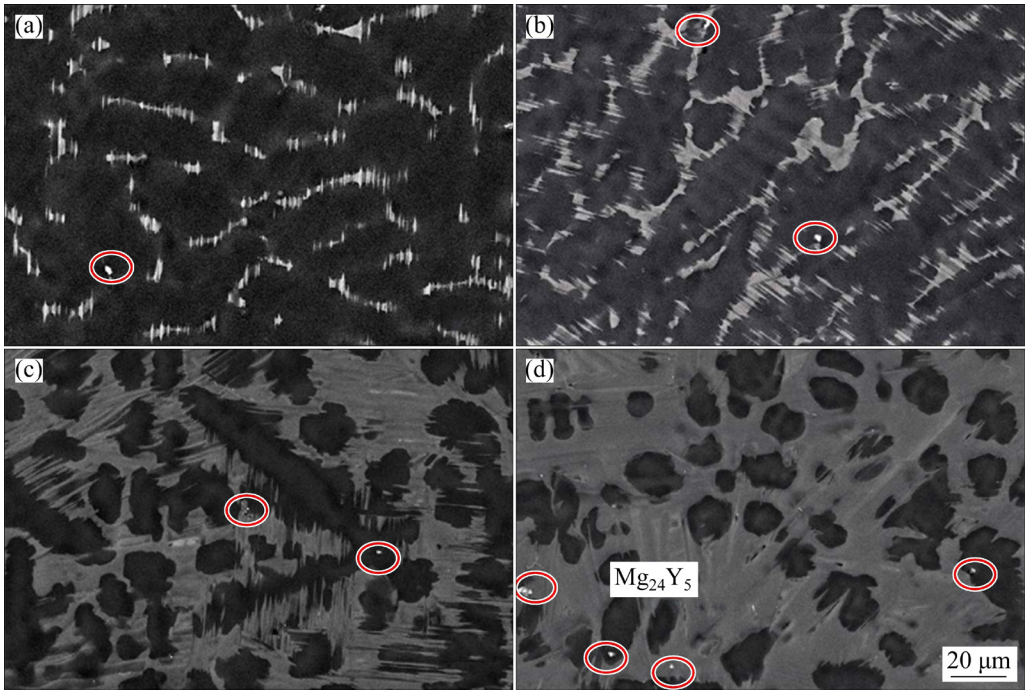

Fig. 1 Backscattered electron micrographs of as-cast Mg−Zn−Y alloys with different compositions: (a) Alloy 1#; (b) Alloy 2#; (c) Alloy 3#; (d) Alloy 4#

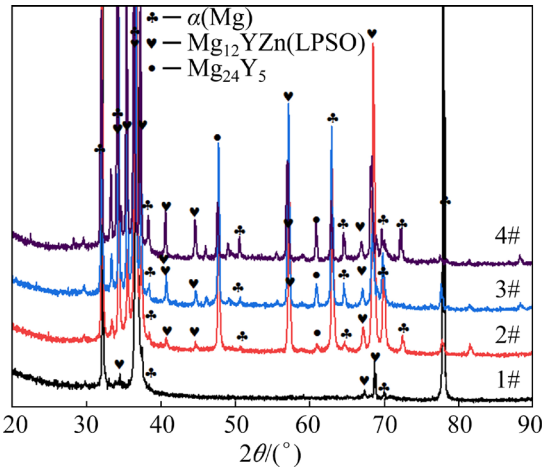

Fig. 2 Calibration of XRD patterns of four as-cast Mg−Zn−Y alloys

large number of gas bubbles uniformly formed on the surfaces of the 1#, 2# and 3# alloys. Although there were relatively less gas bubbles on the surface of the 4# alloy, there were several stable gas columns (as indicated by the arrows). The bubbles are hydrogen gas bubbles resulting from corrosion attack of the alloys. The formation of gas bubbles on the sample surface indicated that uniform corrosion occurred on the alloy surface and the corrosion rate was low. The decreased number of gas bubbles and the formation of gas columns on the surface of the 4# alloy indicated that localized corrosion started to develop on the alloy. In other words, localized corrosion occurred in 4# alloy even at the initial stage of immersion. When the immersion time was extended to 10 min, the number of gas bubbles on the surface of 1#, 2# and 3# alloys decreased and the size of the bubbles increased, particularly for the 1# alloy. In addition, severe localized corrosion sites were observed on 1# and 2# alloys (as indicated by the arrow). At this moment, no localized corrosion sites were observed on the surface of the 3# alloy. For the 4# alloy, although the localized corrosion sites that were initiated earlier did not propagated further, new localized corrosion sites appeared in other locations. After immersion for 30 min, the number and size of

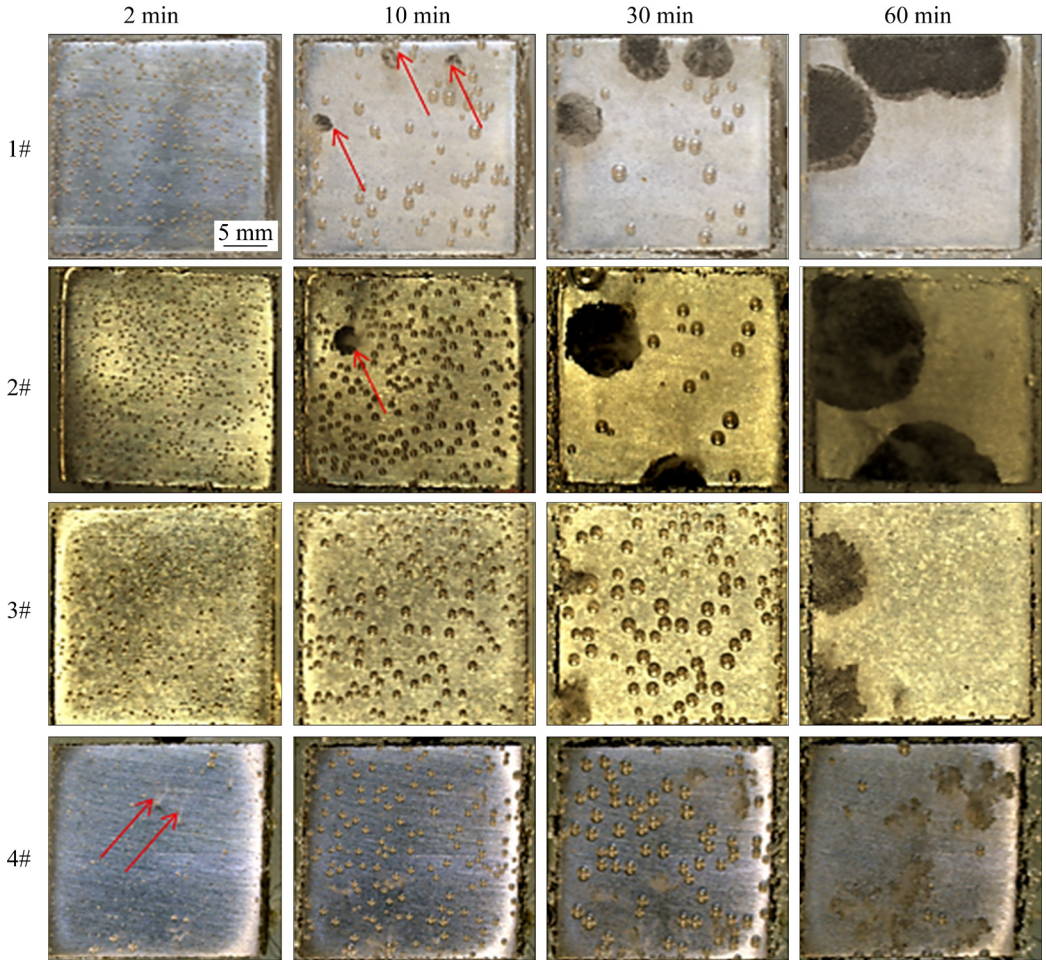

Fig. 3 Macroscopic corrosion morphologies of four alloys in 3.5 wt.% NaCl solution

the gas bubbles on the surface of 1# and 2# alloys decreased further, which was accompanied by significant propagation of localized corrosion. At this moment, localized corrosion started to appear on the 3# alloy. Although new localized corrosion sites appeared on the surface of the 4# alloy after immersion for 30 min, the propagation rate of these localized corrosion sites was not as serious as other samples. After immersion for 60 min, the gas bubbles on the surfaces of all the samples almost completely disappeared. Meanwhile localized corrosion propagated further, which was accompanied by strong gas evolution at the localized corrosion sites. At this moment, the uniform corrosion on the surface of the alloy topped, and the corrosion event was completely governed by localized corrosion.

To further evaluate the corrosion resistance of the cast Mg−Zn−Y alloys, hydrogen evolution test and mass loss test were carried out, with the results shown in Fig. 4. According to Fig. 4, 4# alloy showed the highest corrosion rate, followed by 2# and 1# alloys; and 3# alloy showed the lowest corrosion rate. Besides, it can be seen from Figs. 4(a) and (b) that the initial corrosion rates of the four alloys were relatively low and the corrosion began to accelerate after immersion for 4 h. It was noted that the long-term corrosion behavior shown in Fig. 4 was slightly different from the short-term corrosion behavior suggested in Fig. 3. This will be discussed later.

In order to understand the corrosion mechanism of the alloys during the immersion test, the surface morphology of the sample surface after immersion was observed by SEM (the corrosion products were removed). Figure 5 shows a typical SEM image of the 1# alloy after immersion in 3.5 wt.% NaCl solution for 30 min, at low magnification. The Mg matrix was relatively smooth, with some filamentous features connecting LPSO phases where localized corrosion occurred. At increased magnification (the inset in Fig. 5), it was found that there were some nano-scale pits on the alloy matrix, and the filamentous features were actually some shallow and long grooves. Based on the observation in Figs. 3 and 5, it can be inferred that uniform corrosion occurred on the alloy surface in the early stages of the immersion test, leading to the formation of a corrosion products layer on the alloy surface. At the same time, the galvanic

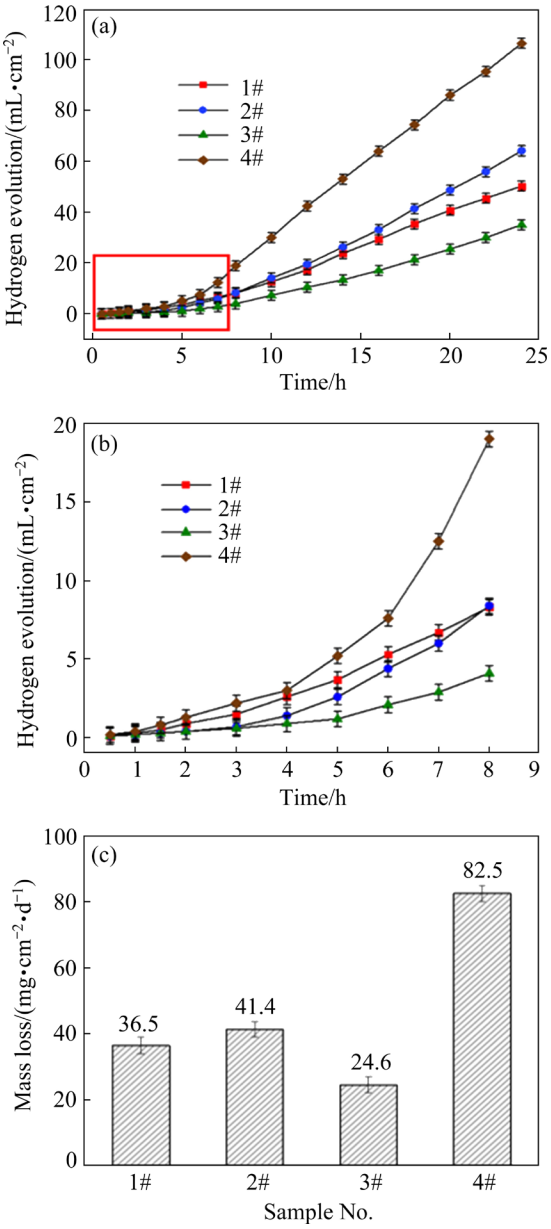

Fig. 4 Hydrogen evolution and mass loss of four alloys in 3.5 wt.% NaCl solution: (a) 24 h hydrogen evolution; (b) 8 h hydrogen evolution; (c) 24 h mass loss

Fig. 5 SEM image showing corrosion morphology of $MgZn_{0.5}Y_{0.67}$ alloy after immersing in 3.5 wt.% NaCl solution for 30 min

coupling effect between the LPSO phase and the alloy matrix promoted the initiation of local corrosion. When the corrosion products layer reached a critical thickness, it provided necessary conditions for the initiation of filiform corrosion, probably around the LPSO phase where the corrosion event proceeded faster as a result of the galvanic corrosion. This explains why the filamentous features always connected with the corroded LPSO phase. The same corrosion morphology was not observed on other alloys (2#, 3# and 4#) after immersion for 30 min. This is probably because the corrosion products layer on the surfaces of 2#, 3# and 4# alloys did not reach the critical thickness at that moment, and therefore did not trigger typical filiform corrosion.

Figure 6 compares the SEM images of the four alloys after immersion in 3.5 wt.% NaCl solution for 30 min, in regions free of severe localized corrosion. The corrosion morphology of 1# and 2# alloys was different from that of 3# and 4# alloys. For 1# and 2# alloys, small corrosion pits were observed between or in the vicinity of the LPSO phase. Besides, there were almost no traces of mechanical polishing on the surfaces of 1# and 2# alloys. According to Fig. 3, it is believed that the corrosion event was mainly governed by uniform corrosion for 1# and 2# alloys, except for weak galvanic corrosion associated with the LPSO phase. For 3# and 4# alloys, however, evident mechanical polishing traces were observed on the surfaces of the LPSO phase and the corrosion event mainly took place in the alloy matrix, suggesting that the change in volume fraction of the LPSO phase greatly changed the corrosion behavior of the alloys.

Figure 7 shows typical SEM images of the four alloys after immersion in 3.5 wt.% NaCl solution for 30 min, in the regions with severe localized corrosion. Generally speaking, the alloy matrix was preferentially attacked relative to the LPSO phase at localized corrosion sites, regardless of the difference in volume fraction of the LPSO phase. This is because the electrode potential of the LPSO phase is more positive than that of magnesium matrix [23]. Therefore, the LPSO phase will work as the cathode in the galvanic corrosion process, accelerating anodic dissolution of the magnesium matrix which works as the anode. Interestingly, it is noted that many LPSO phase blocks have lamellar corrosion morphology. This is because the atoms in the LPSO phase are in lamellar arrangement, and the Y/Zn-rich lamella are electropositive relative to the Mg-rich lamella and will promote anodic dissolution of the latter. In other words, although the LPSO phase generally

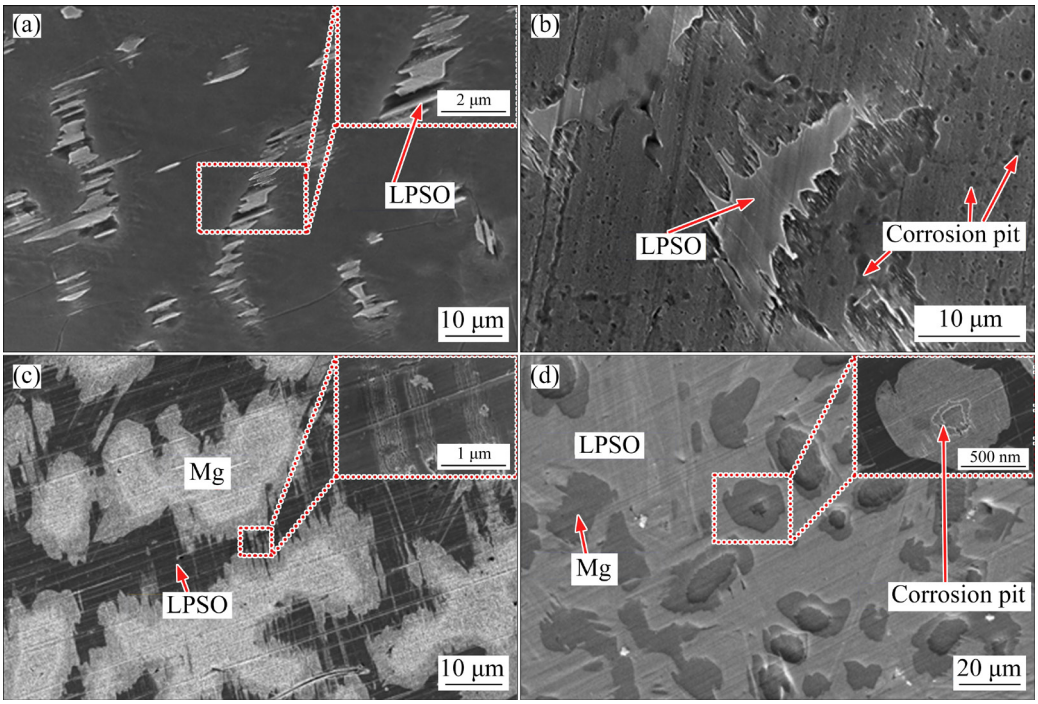

Fig. 6 SEM images of four alloys after immersion in 3.5 wt.% NaCl solution for 30 min (in regions free of severe localized corrosion): (a) 1#; (b) 2#; (c) 3#; (d) 4#

acted as the cathode relative to the magnesium matrix in the corrosion cell, selective corrosion could also occur within the LPSO phase due to the uneven distribution of alloying elements in the LPSO phase.

As revealed in Fig. 7, both the magnesium matrix and the LPSO phase underwent corrosion attack during the immersion process. In order to further understand the corrosion behavior of the four alloys, the cross sections of the alloys after immersion in 3.5 wt.% NaCl solution for 30 min (without removing corrosion products) were observed (Fig. 8). On the surfaces of 1# and 2# alloys, a corrosion product layer of about 1.2 μm in thickness was formed, which was mainly resulted from uniform corrosion of the magnesium matrix.

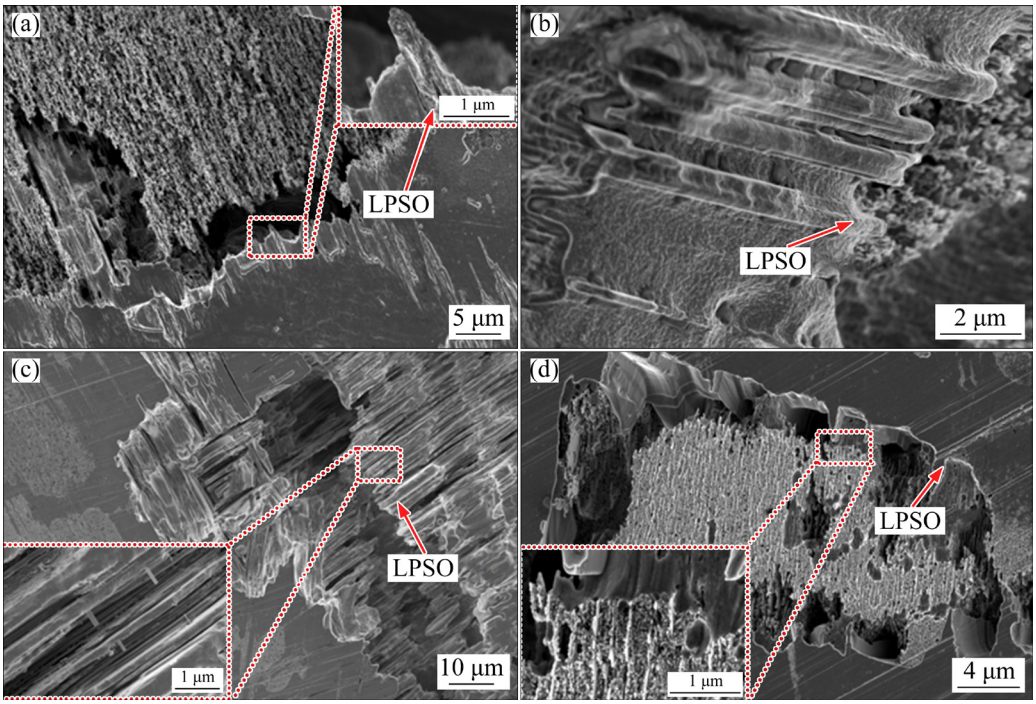

Fig. 7 Microscopic corrosion morphologies of four alloys after immersion in 3.5 wt.% NaCl solution for 30 min (in regions with severe localized corrosion): (a) 1#; (b) 2#; (c) 3#; (d) 4#

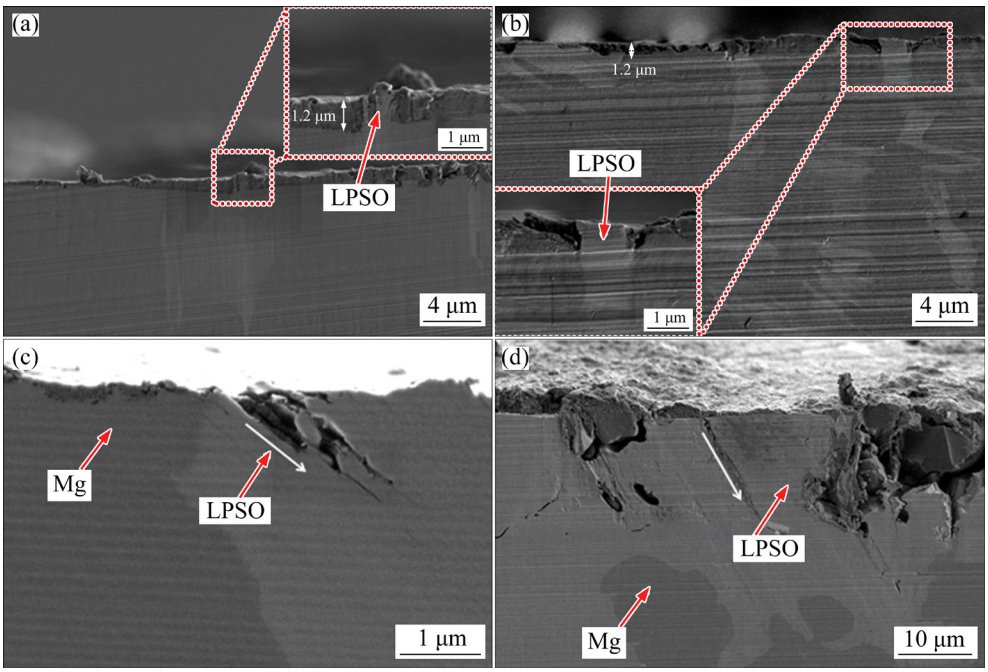

Fig. 8 Cross-sectional morphologies of four alloys after immersion in 3.5 wt.% NaCl solution for 30 min: (a) 1#; (b) 2#; (c) 3#; (d) 4#

There were corrosion trenches around the LPSO phase (insets in Figs. 8(a) and (b)), confirming that the LPSO phase accelerated anodic dissolution of the magnesium matrix. Figure 8(c) shows the typical cross-sectional morphology of 3# alloy. The corrosion products layer on the magnesium matrix was much thinner compared with that on 1# and 2# alloys, suggesting that uniform corrosion proceeded more slowly on the 3# alloy. Interestingly, localized corrosion proceeded along a specific direction within the LPSO phase (as indicated by the arrow in Fig. 8(c)). This is due to selective corrosion attack of the Mg-rich layers in the LPSO phase. Figure 8(d) shows the typical cross-section morphology of the 4# alloy, revealing that the alloy matrix exposed to the specimen surface was seriously corroded and the corrosion fronts finally stopped at the Mg/LPSO phase interface. Again, selective corrosion of the LPSO phase occurred along a specific direction (as indicated by the arrow in Fig. 8(d)).

3.3 Electrochemical analysis

Figure 9(a) shows the open circuit potential (OCP) of the four alloys recorded during immersion in 3.5 wt.% NaCl solution for up to 1800 s. The OCPs of 1# and 2# alloys increased rapidly in the first 300 s, then decreased slowly before stabilization. In contrast, the OCPs of 3# and 4# alloys increased rapidly in the first 100 s and then increased at reduced rates in the next 700 s before final stabilization. The finally stabilized OCPs decreased in order from 4# to 3#, 2# and 1# alloys (Table 2). For a bare alloy, the rapid increase of the OCP in the initial stages of immersion corresponds to the formation a corrosion products layer on the alloy surface [24]. The increasing rate of the OCP vs. immersion time reflects the formation rate of the corrosion products layer (mainly as a consequence of uniform corrosion). Therefore, it can be inferred from Fig. 9(a) that the corrosion products layers on the surface of 1# and 2# alloys were formed faster and consequently thicker than that on 3# and 4# alloys. This is consistent with the observation in Figs. 3 and 8. With increase of the immersion time, the corrosion event on the alloy surface began to change from uniform corrosion to severe localized corrosion (usually revealed as macroscopic pits). Consequently, a dynamic equilibrium state between formation and breakdown of the corrosion products layer was reached, leading to stabilization of the

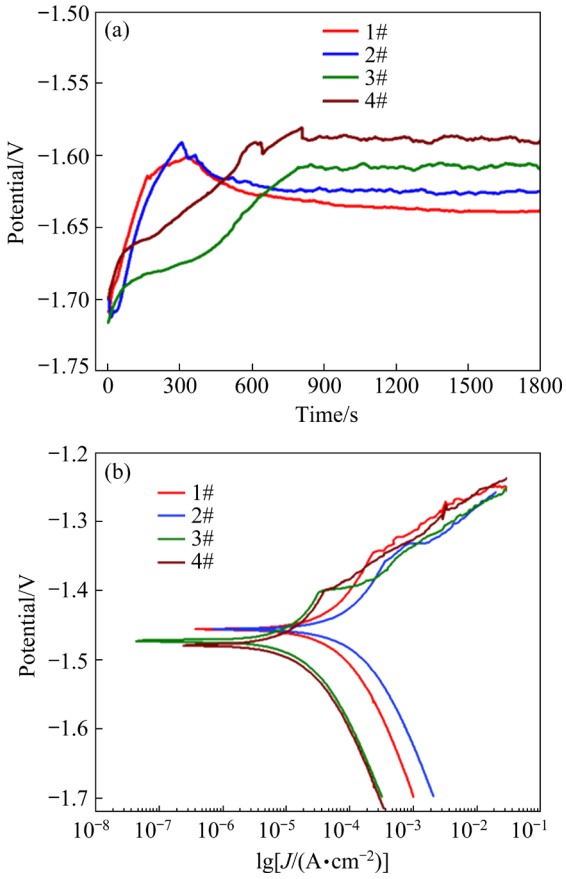

Fig. 9 Open circuit potential (a) and potentiodynamic polarization curves (b) of four alloys in 3.5wt.% NaCl solution

Table 2 Stable open circuit voltages of four alloys after immersing in 3.5 wt.% NaCl solution for 30 min

Alloy	Open circuit voltage/V
1#	−1.64±0.005
2#	−1.62±0.005
3#	−1.60±0.005
4#	−1.58±0.005

OCPs. For 1# and 2# alloys, it took about 300 s to reach the highest OCP, suggesting that the severe localized corrosion was initiated after 300 s of immersion. For 3# and 4# alloys, however, it took about 800 s to reach the highest OCP, suggesting that the severe localized corrosion was initiated in relatively later stages compared with 1# and 2# alloys. This is consistent with macroscopic corrosion morphology observation in Fig. 3. The relatively low increasing rate of the OCP between 100 and 800 s, for 3# and 4# alloys, was probably related to the increased volume fraction of LPSO phase. For the two alloys, the volume fraction of the

LPSO phase was more than 50%. Therefore, the LPSO phase would also greatly influence the OCP. As shown in Fig. 8, there were almost no corrosion products on the surface of the LPSO phase except localized corrosion occurred between the lamella of the LPSO phase. Therefore, the contribution of the LPSO phase to the increase of the OCP was much less than that of the Mg matrix, leading to lower increasing rate of the OCP. The value of the finally stabilized OCP was related to the mixed potential of the alloy surface. Since the standard electrode potential of Y/Y^{3+} (−2.37 V) is similar to that of Mg/Mg^{2+} (−2.37 V), while the standard electrode potential of Zn/Zn^{2+} (−0.76 V) is much higher than that of the other two elements, the higher the Zn content in the alloy, the higher the mixing potential on the alloy surface would be.

Figure 9(b) shows the potentiodynamic polarization curves of the four alloys in 3.5 wt.% NaCl solution. The corrosion potentials and corrosion current densities of the four alloys obtained by Tafel fitting are listed in Table 3. According to Fig. 9(b) and Table 3, the 3# and 4# alloys showed better corrosion resistance than 1# and 2# alloys, which is consistent with the immersion test. Additionally, the cathodic current densities of 3# and 4# were smaller than those of 1# and 2# alloys. The is probably related to the fast formation of the corrosion product layer on the 1# and 2# alloys.

Table 3 Corrosion potentials and corrosion current densities of four alloys obtained by Tafel fitting of potentiodynamic polarization curves

Alloy	φ_{corr}(vs SCE)/V	J_{corr}/(A·cm^{-2})
1#	−1.454±0.002	(1.73±0.05)×10^{-5}
2#	−1.453±0.002	(2.80±0.05)×10^{-5}
3#	−1.475±0.002	(4.32±0.05)×10^{-6}
4#	−1.478±0.002	(5.42±0.05)×10^{-6}

Figure 10 shows the electrochemical impedance spectra of the four alloys after immersion in 3.5 wt.% NaCl solution for 5 min. The equivalent circuit shown in Fig. 11 was used to fit the electrochemical impedance spectra. R_s refers to the solution resistance, R_{ct} and Q_{dl} refer to the charge transfer resistance from the alloy surface to the solution and the double electric layer capacitance at the interface between magnesium

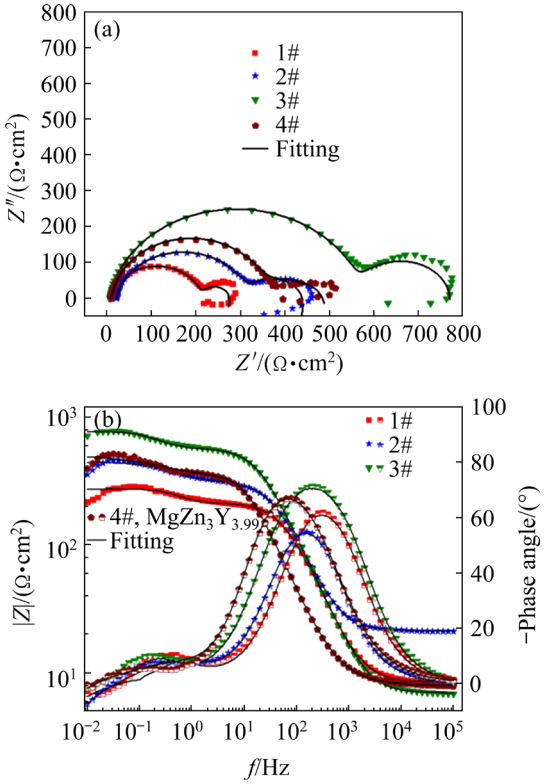

Fig. 10 Electrochemical impedance spectra of four alloys in 3.5 wt.% NaCl solution: (a) Nyquist diagram; (b) Bode diagram

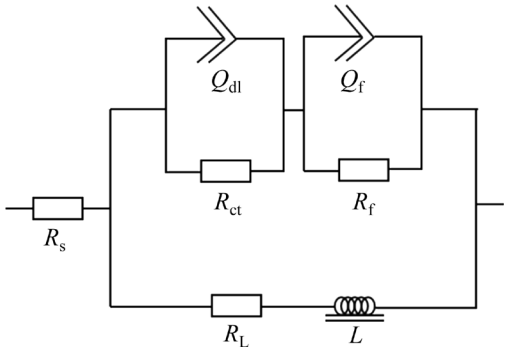

Fig. 11 Equivalent circuit used to fit EIS shown in Fig. 10

matrix and solution (capacitance ring in the high frequency region). Q is a constant phase element defined by two parameters of Y and n, replacing the ideal capacitor to compensate for the heterogeneity on the alloy surface. Q represents a capacitor when n=1 and a resistance when n=0. R_f and Q_f are film resistor and capacitor (capacitor rings in the mid-frequency region), respectively. The inductor L and resistor R_L describe the resistance (inductance ring in low frequency region) that breaks down the protective film under the influence of adsorption

reaction of Mg^{2+} and H_2O, reflecting the onset of localized corrosion. The values of each component after fitting are shown in Table 4. The R_{ct} value decreased in order as 3# > 4# > 1# > 2#, suggesting that 3# alloy had the lowest corrosion rate while 2# alloy had the highest corrosion rate; the R_f value decreased in order as 1# > 2# > 4# > 3#, suggesting that 1# alloy had the thickest corrosion products layer while 3# alloy had the thinnest corrosion products layer. The EIS results well agree with the immersion test and the potentiodynamic polarization test.

4 Discussion

In this work, according to the formation of the minimum structural unit of the 18R-LPSO phase, namely Zn/Y=3/4, four Mg−Zn−Y alloys were designed by changing the absolute contents of Zn and Y. Through the design, the composition of the magnesium solid solution was similar while the volume fraction of the 18R-LPSO phase increased with the increase of the alloying contents. Consequently, the influence of different volume fractions of the 18R-LPSO phase on the corrosion behavior of Mg−Zn−Y alloys could be investigated by comparing the corrosion behavior of the four alloys.

When the volume fraction of the LPSO phase is relatively small (e.g. 1# and 2# alloys), the LPSO phase mainly exists in form of discrete blocks, and the corrosion process of the alloy is mainly controlled by the corrosion process of the magnesium solid solution. When the alloy is exposed to corrosive medium, a relatively uniform and continuous corrosion products layer will be formed rapidly on the alloy surface. At the same time, the galvanic coupling between the alloy matrix and the LPSO phase results in initiation of localized corrosion at the LPSO/ alloy matrix interface. Once the corrosion products layer reaches a critical thickness, filiform corrosion will develop under the corrosion products layer, leading to propagation of localized corrosion. In this case, the corrosion resistance of the alloy decreases with the increase of the volume fraction of the LPSO phase, because the increased number of LPSO blocks means increased number of corrosion cells and therefore higher corrosion rate.

When the volume fraction of LPSO phase increases to about 50% (e.g. 3# alloy), the effect of the LPSO phase on uniform corrosion of alloy cannot be ignored. At the initial stage of corrosion, the corrosion products layer is formed rapidly on the alloy matrix. With thickening of the corrosion products layer on the surface of the exposed alloy matrix, the LPSO phase might become anodic relative to the corroded alloy matrix, which will promote selective attack of the LPSO phase along the Mg-rich layers. The corrosion of the LPSO phase will then inhibit uniform corrosion of the alloy matrix and the thickening of the corrosion products layer. The mutual polarization between the alloy matrix and the LPSO phase consequently postpones the occurrence of severe localized corrosion. This explains why 3# alloy showed relatively high corrosion resistance.

When the volume fraction of the LPSO phase is much larger than 50% (e.g. 4# alloy), the anodic dissolution of the alloy matrix becomes severe even in early stages of the immersion test due to strong galvanic coupling effect between the LPSO phase and the alloy matrix. However, since a complete LPSO phase network has been formed, the anodic dissolution of the alloy matrix will be slowed down when the corrosion front reaches the LPSO phase. After that, the corrosion of the alloy mainly occurs within the LPSO phase along the Mg-rich layers, and the corrosion rate will evidently decrease. In this sense, the corrosion resistance of the alloy can be greatly improved if the volume fraction of the LPSO phase is near 100%.

Table 4 Parameters obtained by fitting EIS using equivalent circuit shown in Fig. 11

Alloy	R_s/ ($\Omega\cdot cm^2$)	R_L/ ($\Omega\cdot cm^2$)	L/ ($H\cdot cm^2$)	Y_f/ ($\mu\Omega^{-1}\cdot cm^{-2}\cdot s^n$)	n_f/	R_f/ ($\Omega\cdot cm^2$)	Y_{dl}/ ($\mu\Omega^{-1}\cdot cm^{-2}\cdot s^n$)	n_{dl}/	R_{ct}/ ($\Omega\cdot cm^2$)
1#	8.50	266	4.85×10^4	2.99×10^{-4}	1	6690	9.17×10^{-1}	0.91	805
2#	8.12	106	4.47×10^4	2.50×10^{-5}	0.91	2920	4.16×10^{-2}	0.86	131
3#	8.01	764	6.74×10^5	2.34×10^{-5}	0.92	192	3.12×10^{-4}	0.97	1020
4#	7.90	787	1.15×10^5	4.75×10^{-5}	1	520	1.56×10^{-3}	0.63	811

However, it should be pointed out that such deduction is only true for short-term corrosion exposure (e.g. up to 60 min). As suggested in Fig. 4, the 4# alloy had the highest corrosion resistance after prolonged exposure. It is believed that the continuous LPSO phase in the 4# alloy somehow collapsed after immersion in the NaCl for 24 h. This deduction is supported by examining the corrosion products (Figs. 12(a−c)). Figure 12(a) shows the SEM image of the corrosion product, revealing block features. EDS analysis of the block features shows high contents of O, Mg, Zn, and Y elements (Fig. 12(b)). XRD analysis of the corrosion products shows strong diffraction peaks of LPSO phase (Fig. 12(c)), confirming that the block features shown in Fig. 12(a) are mainly LPSO phase particles. Based on these observations, the corrosion process of the 4# alloy after prolonged exposure in the NaCl solution is schematically illustrated in Fig. 12(d). Initially, the magnesium matrix is selectively attacked, leaving the LPSO networks. As suggested in Fig. 8, selective attack of the LPSO phase will also occur along the Mg-rich layers in the LPSO phase. Given sufficient exposure time, the corrosion fronts might pass through the LPSO phase and reach the magnesium matrix beneath the corroded LPSO phase. Again, the magnesium matrix would be preferentially attacked. In this case, the narrow corrosion path in the LPSO phase would work as paths for ion and mass diffusion, which provides the conditions for the formation of occluded corrosion cells. The corrosion attack of the magnesium matrix beneath the LPSO phase results in acidification in the bottom of the occluded corrosion cell, further promoting corrosion attack of the magnesium matrix and the Mg-rich layers in the LPSO phase. The magnesium matrix is corroded much faster than the LPSO phase, leading to collapse of the remained LPSO phase particle. Afterwards, such process repeats. This explains why the 4# alloy was corroded at relatively lower rate in early stages of immersion while at much higher rate after prolonged exposure. Furthermore, with the increase of volume fraction of the LPSO phase, the comprehensive mechanical properties of the alloy will decrease significantly [25,26]. Therefore, considering both the corrosion resistance and mechanical properties, it is expected that the Mg−Zn−Y with volume fraction of the LPSO phase being close to 50% might show good comprehensive properties.

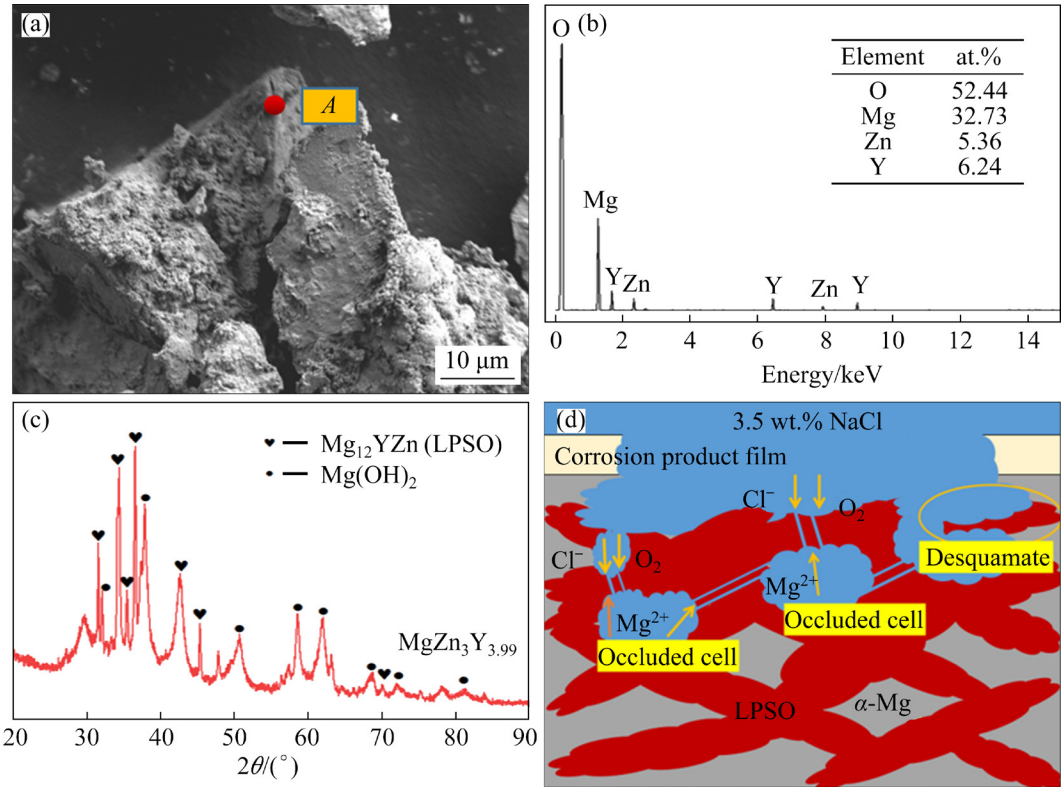

Fig. 12 SEM image of corrosion products on 4# alloy after immersion in 3.5% NaCl solution for 24 h (a), EDS analysis of corrosion products (b), XRD analysis of corrosion products (c), and schematic illustration of corrosion process (d)

5 Conclusions

(1) Four cast Mg−Zn−Y alloys with different volume fraction of the 18R-LPSO phase, namely 16.55%, 34.45%, 54.24% and 70.36%, were successfully prepared. The morphology of the LPSO phase changed from discrete blocks to continuous networks with the increase of the Zn and Y contents. The Mg−Zn−Y alloy with 54.24% of the LPSO phase showed the best corrosion resistance in 3.5 wt.% NaCl solution.

(2) The volume fraction and, consequently, the distribution of the LPSO phase greatly affected the corrosion resistance of the Mg−Zn−Y alloys in 3.5 wt.% NaCl solution. The Mg−Zn−Y alloys would undergo uniform corrosion in the early stage of the immersion test; the uniform corrosion was gradually replaced by filiform corrosion or other forms of localized corrosion with further exposure. The alloy with 54.24% of the LPSO phase showed the best corrosion resistance while the alloy with 70.36% of the LPSO phase showed the worst corrosion resistance.

(3) The LPSO phase was cathodic relative to the alloy matrix, promoting anodic dissolution of the alloy matrix surrounding it. However, selective corrosion attack also occurred along the Mg-rich layer within the LPSO phase during the immersion test, especially for the alloys with relatively large volume fraction of the LPSO phase.

Acknowledgments

This work was supported by Chongqing Talent Plan: Leading Talents in Innovation and Entrepreneurship, China (No. CQYC201903051), University Innovation Research Group of Chongqing, China (No. CXQT20023), Qingnian Project of Science and Technology Research Program of Chongqing Municipal Education Commission, China (No. KJQN202001106), China Postdoctoral Science Foundation (No. 2021M700556), Natural Science Foundation of Chongqing, China (No. cstc2021jcyj-bshX0114), Natural Science Foundation of China (Nos. U20A20234, 51874062), and Chongqing Foundation and Advanced Research Project, China (No. cstc2019jcyj- zdxmX0010).

References

[1] LIU Huan, HUANG He, WANG Ce, SUN Jia-peng, BAI Jing, XUE Feng, MA Ai-bin, CHEN Xiao-Bo. Recent advances in LPSO-containing wrought magnesium alloys: Relationships between processing, microstructure and mechanical properties [J]. JOM, 2019, 71(9): 3314−3327.

[2] YANG Yan, XIONG Xiao-ming, CHEN Jing, PENG Xiao-dong, CHEN Dao-lun, PAN Fu-sheng. Research advances in magnesium and magnesium alloys worldwide in 2020 [J]. Journal of Magnesium and Alloys, 2021, 9(3): 705−747.

[3] LUKYANOVA E A, ROKHLIN L L, TABACHKOVA N Y, DOBATKINA T V, NIKITINA N I. Reversion after ageing in an Mg−Y−Gd−Zr alloy [J]. Journal of Alloys and Compounds, 2015, 635: 173−179.

[4] SONG Jiang-feng, SHE Jia, CHEN Dao-lun, PAN Fu-sheng. Latest research advances on magnesium and magnesium alloys worldwide [J]. Journal of Magnesium and Alloys, 2020, 8(1): 1−41.

[5] DING Zhi-bing, ZHAO Yu-hong, LU Rui-peng, YUAN Mei-ni, WANG Zhi-jun, LI Hong-jun, HUO Hua. Effect of Zn addition on microstructure and mechanical properties of cast Mg−Gd−Y−Zr alloys [J]. Transactions of Nonferrous Metals Society of China, 2019, 29(4): 722−734.

[6] SOMEKAWA H, ANDO D, HAGIHARA K, YAMASAKI M, KAWAMURA Y. Intrinsic kink bands strengthening induced by several wrought-processes in Mg−Y−Zn alloys containing LPSO phase [J]. Materials Characterization, 2021, 179: 111348.

[7] LUO S Q, TANG A T, JIANG B, LIU W J, CHENG R J, PAN F S. The element features and criterion of formation of LPSO in magnesium alloys [J]. Materials Research Innovations, 2015, 19 (S4): s133−s137.

[8] HAGIHARA K, KINOSHITA A, SUGINO Y, YAMASAKI M, KAWAMURA Y, YASUDA H Y, UMAKOSHI Y. Plastic deformation behavior of $Mg_{97}Zn_1Y_2$ extruded alloys [J]. Transactions of Nonferrous Metals Society of China, 2010, 20(7): 1259−1268.

[9] BAZHENOV V E, SAIDOV S S, TSELOVALNIK Y V, VOROPAEVA O O, PLISETSKAYA I V, TOKAR A A, BAZLOV A I, BAUTIN V A, KOMISSAROV A A, KOLTYGIN A V, BELOV V D. Comparison of castability, mechanical, and corrosion properties of Mg−Zn−Y−Zr alloys containing LPSO and W phases [J]. Transactions of Nonferrous Metals Society of China, 2021, 31(5): 1276−1290.

[10] XU Shi-yuan, LIU Chu-ming, WAN Ying-chun, ZENG Guang, GAO Yong-hao, JIANG Shu-nong. Corrosion behaviour of Mg−Gd−Y−Zn−Ag alloy components with different sizes after cooling [J]. Transactions of Nonferrous Metals Society of China, 2021, 31(5): 1291−1302.

[11] FUJITA N, YAMASHITA K, MATSUSHITA M, YAMASAKI M, KAWAMURA Y, ABE E. B22-P-12 A novel long-period structure formed in a high-pressure synthesized Mg−Zn−Yb alloy [J]. Microscopy, 2015, 64 (S1): i108−i108.

[12] INOUE A, KAWAMURA Y, MATSUSHITA M, HAYASHI

K, KOIKE J. Novel hexagonal structure and ultrahigh strength of magnesium solid solution in the Mg−Zn−Y system [J]. Journal of Materials Research, 2001, 16(7): 1894−1900.

[13] HAGIHARA K, KINOSHITA A, SUGINO Y, YAMASAKI M, KAWAMURA Y, YASUDA H Y, UMAKOSHI Y. Effect of long-period stacking ordered phase on mechanical properties of $Mg_{97}Zn_1Y_2$ extruded alloy [J]. Acta Materialia, 2010, 58(19): 6282−6293.

[14] GARCES G, PEREZ P, CABEZA S, KABRA S, GAN W, ADEVA P. Effect of extrusion temperature on the plastic deformation of an Mg−Y−Zn alloy containing LPSO phase using in situ neutron diffraction [J]. Metallurgical and Materials Transactions A, 2017, 48(11): 5332−5343.

[15] LIU Jing, YANG Li-xin, ZHANG Chun-yan, ZHANG Bo, ZHANG Tao, LI Yang, WU Kai-ming, WANG Fu-hui. Role of the LPSO structure in the improvement of corrosion resistance of Mg−Gd−Zn−Zr alloys [J]. Journal of Alloys and Compounds, 2019, 782: 648−658.

[16] WANG Yu-jiao, ZHANG Yun, WANG Pan-pan, ZHANG Dan, YU Bo-wen, XU Zhe, JIANG Hai-tao. Effect of LPSO phases and aged-precipitations on corrosion behavior of as-forged $MgGd_6Y_2Zn_1Zr_{0.3}$ alloy [J]. Journal of Materials Research and Technology, 2020, 9(4): 7087−7099.

[17] SRINIVASAN A, HUANG Y, MENDIS C L, BLAWERT C, KAINER K U, HORT N. Investigations on microstructures, mechanical and corrosion properties of Mg−Gd−Zn alloys [J]. Materials Science and Engineering A, 2014, 595: 224−234.

[18] WANG Li-sha, JIANG Jing-hua, LIU Huan, SALEH B, MA Ai-bin. Microstructure characterization and corrosion behavior of Mg−Y−Zn alloys with different long period stacking ordered structures [J]. Journal of Magnesium and Alloys, 2020, 8(4): 1208−1220.

[19] ITAKURA M, YAMAGUCHI M, EGUSA D, ABE E. Density functional theory study of solute cluster growth processes in Mg−Y−Zn LPSO alloys [J]. Acta Materialia, 2021, 203: 116491.

[20] HOSOKAWA S, STELLHORN J R, PAULUS B, MARUYAMA K, KOBAYASHI K, OKUDA H, YAMASAKI M, KAWAMURA Y, SATO H. The seeds of Zn_6Y_8 L12-type clusters in amorphous $Mg_{85}Zn_6Y_9$ alloy investigated by photoemission spectroscopy [J]. Journal of Alloys and Compounds, 2018, 764: 431−436.

[21] YIN Si-qi, DUAN Wen-chao, LIU Wen-hong, WU Liang, BAO Jia-xin, YU Jia-ming, LI Liang, ZHAO Zhong, CUI Jian-zhong, ZHANG Zhi-qiang. Improving the corrosion resistance of $MgZn_{1.2}Gd_xZr_{0.18}$ (x=0, 0.8, 1.4, 2.0) alloys via Gd additions [J]. Corrosion Science, 2020, 177: 108962.

[22] CHENG Peng, ZHAO Yu-hong, LU Ruo-peng, HOU Hua. Effect of the morphology of long-period stacking ordered phase on mechanical properties and corrosion behavior of cast Mg−Zn−Y−Ti alloy [J]. Journal of Alloys and Compounds, 2018, 764: 226−238.

[23] LI C Q, XU D K, ZENG Z R, WANG B J, SHENG L Y, CHEN X B, HAN E H. Effect of volume fraction of LPSO phases on corrosion and mechanical properties of Mg−Zn−Y alloys [J]. Materials & Design, 2017, 121: 430−441.

[24] WANG Nai-guang, WANG Ri-chu, PENG Chao-qun, FENG Yan, ZHANG Xiang-yu. Corrosion behavior of Mg−Al−Pb and Mg−Al−Pb−Zn−Mn alloys in 3.5% NaCl solution [J]. Transactions of Nonferrous Metals Society of China, 2010, 20: 1936−1943.

[25] TONG L B, LI X H, ZHANG H J. Effect of long period stacking ordered phase on the microstructure, texture and mechanical properties of extruded Mg–Y–Zn alloy [J]. Materials Science and Engineering: A, 2013, 563: 177−183.

[26] TANG Y X, Li B, TANG H X, XU Y C, GAO Y P, WANG L H, GUAN J Y. Effect of long period stacking ordered structure on mechanical and damping properties of as-cast Mg–Zn–Y–Zr alloy [J]. Materials Science and Engineering: A, 2015, 640: 287−294.

18R-LPSO 相的体积分数对 Mg−Zn−Y 合金腐蚀行为与机理的影响

席国强[1]，牟 宇[1]，麻彦龙[1]，赵旭晗[1]，熊 菊[1]，马 凯[2]，王敬丰[2]

1. 重庆理工大学 材料科学与工程学院，重庆 400054；
2. 重庆大学 材料科学与工程学院，重庆 400044

摘 要：通过实验设计阐明 LPSO 相对镁合金腐蚀行为的影响。按照形成 18R-LPSO 相的最小结构单元，即 Zn/Y=3/4(摩尔比)，设计 4 种不同 LPSO 相体积分数的 Mg−Zn−Y 合金，对比研究 4 种合金的显微组织和腐蚀行为。结果表明，合金主要含有 α-Mg 和 18R-LPSO 相，18R-LPSO 相的体积分数随着 Zn 和 Y 含量的增加而增加。4 种合金中 18R-LPSO 相的体积分数依次为 16.55%、34.45%、54.24%和 70.36%，18R-LPSO 相的空间分布也由离散块状变为连续网络状。当 LPSO 相的体积分数在 50%左右时，合金的耐蚀性最好，体积分数大于或小于 50%都会导致合金耐蚀性能降低。

关键词：Mg−Zn−Y 合金；18R-LPSO 相；体积分数；耐腐蚀性能

(Edited by Xiang-qun LI)